

ARTICLE

From spores to fungal pellets: A new high-throughput image analysis highlights the structural development of *Aspergillus niger*

Henri Müller¹  | Lars Barthel²  | Stefan Schmieder¹  | Tabea Schütze²  | Vera Meyer²  | Heiko Briesen¹ 

¹Department of Process Systems Engineering, School of Life Sciences Weihenstephan, Technical University of Munich, Freising, Germany

²Department of Applied and Molecular Microbiology, Institute of Biotechnology, Technische Universität Berlin, Berlin, Germany

Correspondence

Vera Meyer, Department of Applied and Molecular Microbiology, Technische Universität Berlin, Straße des 17. Juni 135, 10623 Berlin, Germany.
Email: vera.meyer@tu-berlin.de

Heiko Briesen, Department of Process Systems Engineering, Technical University of Munich, Gregor-Mendel-Str. 4, 85354 Freising, Germany.
Email: heiko.briesen@tum.de

Funding information

Deutsche Forschungsgemeinschaft, Grant/Award Numbers: 315305620, 315384307, 427889137

Abstract

Many filamentous fungi are exploited as cell factories in biotechnology. Cultivated under industrially relevant submerged conditions, filamentous fungi can adopt different macromorphologies ranging from dispersed mycelia over loose clumps to pellets. Central to the development of a pellet morphology is the agglomeration of spores after inoculation followed by spore germination and outgrowth into a pellet population, which is usually very heterogeneous. As the dynamics underlying population heterogeneity is not yet fully understood, we present here a new high-throughput image analysis pipeline based on stereomicroscopy to comprehensively assess the developmental program starting from germination up to pellet formation. To demonstrate the potential of this pipeline, we used data from 44 sampling times harvested during a 48 h submerged batch cultivation of the fungal cell factory *Aspergillus niger*. The analysis of up to 1700 spore agglomerates and 1500 pellets per sampling time allowed the precise tracking of the morphological development of the overall culture. The data gained were used to calculate size distributions and area fractions of spores, spore agglomerates, spore agglomerates within pellets, pellets, and dispersed mycelia. This approach eventually enables the quantification of culture heterogeneities and pellet breakage.

KEYWORDS

Aspergillus niger, image analysis, morphology development, pellet growth, spore agglomeration/aggregation

1 | INTRODUCTION

The birth of industrial biotechnology dates back to the start of citric acid production using the filamentous fungus *Aspergillus niger* more than 100 years ago. Ever since, filamentous fungi played an important role in many industrial processes and are nowadays of central importance to establish a future circular economy (Cairns et al., 2018;

V. Meyer et al., 2020). Filamentous fungi are used as cell factories for a diverse range of products, for example, drugs, enzymes, organic acids, or commodities for the pharma, feed, food, fuel, textile, and chemical industries (V. Meyer et al., 2020). During submerged cultivation, spores and hyphae from filamentous fungi develop into different macromorphologies ranging from dispersed mycelium to pellets. Contrary to dispersed mycelia (freely dispersed hyphae) and

This is an open access article under the terms of the Creative Commons Attribution-NonCommercial License, which permits use, distribution and reproduction in any medium, provided the original work is properly cited and is not used for commercial purposes.

© 2022 The Authors. *Biotechnology and Bioengineering* published by Wiley Periodicals LLC.

clumps (loose agglomerates of hyphae), fungal pellets are dense spherical hyphal networks with a diameter between a few hundred micrometers and some millimeters (Cairns et al., 2019; Cox et al., 1998). The developed macromorphological structure of fungal production strains greatly influences the productivity of the bioprocess (Tegelaar et al., 2020; Veiter et al., 2018). Higher viscosity and a non-Newtonian behavior characterize the cultivation processes of dispersed mycelia compared to pellets. Therefore, less energy is required to mix a cultivation of pellets and hence lower shear stress is applied. Furthermore, homogeneous mass transfer of substrates and especially oxygen into the medium and from the bulk phase to the pellets is favorably enhanced (Gibbs et al., 2000). However, the diffusivity of oxygen inside fungal pellets depends on the hyphal density (Schmideder et al., 2019, 2020). Dense hyphal structures can result in oxygen-limited regions in the center of fungal pellets, resulting in growth limitation and reduced growth-associated product formation (Driouch et al., 2010; Hille et al., 2009). Posch et al. (2012) observed a diffusion-limiting compactness after 15 h of pelleted growth of *Penicillium chrysogenum*. Different strategies have thus been developed to increase the productivity of bioprocesses by altering fungal macromorphologies. Most of them focus on the variation of the cultivation conditions, including medium composition, pH and osmolality of the medium, spore inoculum concentration, viability/vitality of the inoculum, bioreactor geometry, shear stress, aeration rate, temperature, and the addition of microparticles to name but a few (Böl et al., 2021; Driouch et al., 2010; Kaup et al., 2008; Laible et al., 2021; Papagianni, 2004; Wucherpfennig et al., 2010, 2011). Genetic factors and intracellular processes that affect or even control spore germination, hyphal growth, and eventually pellet formation can be grouped into cytoskeletal networks, exocytosis, endocytosis, cell membrane, and cell wall biogenesis. They jointly define hyphal growth and hyphal surface properties, and thus contribute to the development of macromorphologies (for recent reviews, see Cairns et al., 2019; Commer & Shaw, 2020; Miyazawa et al., 2020). Remarkably, systems biology data and gene coexpression networks nowadays allow the prediction and modification of genes to be important for fungal macromorphological developments (Cairns et al., 2019; Fiedler, Cairns, et al., 2018).

In general, pellet formation can be classified into either coagulative or noncoagulative processes (Veiter et al., 2018). During coagulative pellet formation (representatives are *A. niger*, *Aspergillus nidulans*, or *Penicillium oxalicum*), spores agglomerate after inoculation due to electrostatic and salt bridging between cell wall surface polysaccharides and due to hydrophobicity of spore surface proteins (Dynesen & Nielsen, 2003; Pascual et al., 2000; Zhang & Zhang, 2016). During noncoagulative pellet formation (one representative is *Rhizopus oryzae*), single spores form single pellets, that is, spores remain dispersed during germination, but hyphae can agglomerate at later growth phases (Zhang & Zhang, 2016). Notably, the macromorphological development of some fungi follows both the coagulative and noncoagulative processes (a representative is *Penicillium chrysogenum*). Coagulative spore types are also able to form noncoagulative pellets when environmental conditions change, for example, pH increase of the medium (Veiter et al., 2018).

Recently, it was shown that macromorphologies of *A. niger* considerably differed when cultivated in two different bioreactor types (stirred-tank reactor, waved-mixed reactor), although identical medium compositions, feeding schemes, temperature, and pH control were applied (Kurt et al., 2018). Reduced shear stress under wave-mixed conditions provoked the formation of *A. niger* pellets, which were very heterogeneous in size. It was hypothesized that these very heterogeneous pellet populations ensured faster biomass accumulation when compared to stirred-tank cultivations, where homogeneously dispersed mycelia were predominantly formed by *A. niger* (Kurt et al., 2018). Importantly, the mycelial heterogeneity phenomenon is not restricted to filamentous fungi but is also observed in filamentous bacteria including *Streptomyces*, some of which are also well-established cell factories for drug and antibiotics production (Nepal & Wang, 2019). Here, it was shown that heterogeneity is also influenced by germling aggregation in *Streptomyces* spp. (Zacchetti et al., 2016).

Hence, only a deeper and holistic understanding of the interactions as well as interdependencies of process conditions, genetic conditions, and population heterogeneities will pave the way for the rational morphology engineering of filamentous fungi in the future. One central prerequisite to achieve this is the availability of image analysis pipelines that allow the qualitative and quantitative description of different processes including spore agglomeration, pellet formation, pellet growth, pellet breakage events, and to access the extent of population heterogeneity. In particular, the holistic description of the pellet formation processes is of great importance, for example, it is difficult to quantify the influence of different cultivation conditions on the fungi just by analyzing the final fungal morphological state without considering a possibly changed spore agglomeration, which is the first step and one driving factor for the initial formation of pellets.

Existing high-throughput methods to study the structural development of filamentous fungi cultivations, including focused beam reflectance measurement and image analysis, track either the spore agglomeration or the macromorphological pellet development during growth (Cairns et al., 2019; Grimm et al., 2004; Willemse et al., 2018). To the best of our best knowledge, flow cytometry, which can be used for fungal pellet analysis (Bekker et al., 2011; Ehgartner et al., 2017; Schrinner et al., 2020; Tegelaar et al., 2020; Veiter & Herwig, 2019), has never been used to analyze the spore agglomeration and the morphological development of pellets within one cultivation.

In the present study, we aim to track the evolution of pellets and dispersed mycelia in the coagulative-type industrially exploited fungus *A. niger* starting from spore inoculation. To observe and evaluate spore agglomeration, pellet formation, pellet growth, and population heterogeneities, we designed a new fast high-throughput image analysis pipeline based on stereomicroscopic images from culture samples. In doing so, we were able to analyze 2500 fungal objects (spores/spore agglomerates, spore agglomerates within pellets, pellets) on average per sample during cultivation and were able to calculate the size distributions of the detected objects. We

complemented the size distributions by area fractions of the fungal objects including dispersed mycelia to enable complete characterization of the whole cultivation.

2 | MATERIALS AND METHODS

2.1 | Strain and inoculum preparation

We utilized the hyperbranching *A. niger* $\Delta racA$ strain MF22.4 (Fiedler, Barthel, et al., 2018; Kwon et al., 2013). Conidiospores of MF22.4 were obtained from agar plate cultures by using standard procedures for filamentous fungi (Bennet & Lasure, 1991). Ten milliliters of physiological salt solution (PS) were carefully added on top of the well-sporulated plate culture. Subsequently, a cotton stick was used to spread the PS over the plate, while simultaneously using it to scrub the spores from the mycelium. Spores were then filtrated and stored in PS for 17 h at 4°C until inoculation. The PS solution was prepared with 8.9 g/L sodium chloride.

2.2 | Media, cultivation, and sampling

Five-liter Erlenmeyer flasks and 1 L complete medium (V. Meyer et al., 2010) with 9 g/L glucose were used for the submerged cultivation of *A. niger*. The shake flasks were inoculated with 2.5×10^6 spores/ml. *Aspergillus niger* MF22.4 was cultivated for 48 h at 30°C with a rotational speed of 90 RPM in an Infors HT Multitron Standard shaker (Infors AG). The cultivation was performed in duplicate (flasks A and B).

Samples were taken every 30 min for the first 10 h and every hour for the next 22 h. The last sample was taken after 48 h of cultivation, resulting in a total number of 44 sampling times. At each sampling time, stereo and differential interference contrast (DIC) microscopy were performed. The biomass concentration was determined every hour from the sampling time 6 h on. The glucose concentration was determined every second hour.

2.3 | Stereomicroscopy

The main imaging, that is, the method to acquire thousands of fungal objects, was performed with a Leica S8APO stereomicroscope (Leica Microsystems GmbH) connected to a Leica MC120 HD camera (Leica Microsystems GmbH). For image capture, 3 ml of culture volume were carefully pipetted into a Petri dish (Sarstedt AG & Co. KG) with 85 mm inside diameter using a 10 ml serological pipette (Sarstedt AG & Co. KG) and diluted with distilled H₂O until the bottom of the Petri dish was just completely filled with liquid. Care was taken to ensure that there was not too much water in the Petri dish to avoid overlapping of pellets. Further, the Petri dish was gently swirled to separate loosely attached pellets from each other. Subsequently, the Petri dish was put on a blue cardboard with a rectangular grid in the

measurement area of the stereomicroscope (Supporting Information: Figure S1). As the blue cardboard enhanced the contrast, it facilitated the subsequent image analysis. One image per 13×11 mm rectangle and at least 24 images per sampling time were taken by carefully sliding the blue cardboard template together with the Petri dish from rectangle to rectangle while preventing the pellets from moving to avoid double image capture of the same sample area. In total, about 1300 images were taken for each cultivation flask. To depict all structural changes of *A. niger* MF22.4 during submerged cultivation and to bridge the length scale between single spores in the range of a few micrometers and pellets in the range of a few hundred micrometers, the magnification of the stereo microscope was adjusted at certain sampling times. Supporting Information: Table S1 summarizes the isotropic pixel size, the field of view, and sampling times when the magnification was changed. The stereomicroscopic images were saved in an 8-bit RGB JPEG file format.

2.4 | DIC microscopy

To image a few fungal objects per sampling time with higher magnification, a Leica DM 5000 CS (Leica Microsystems GmbH) DIC microscope was used. Per sampling time, 15 μ l of culture volume were transferred on a microscope slide and covered with a cover glass. Twenty to 40 images per sampling time with 100- and 400-fold magnification resulting in pixel sizes of 0.651 and 0.163 μ m, respectively, were taken. The DIC high-resolution images were used to validate the results of our newly developed image analysis pipeline, which is based on the stereomicroscope images.

The stereomicroscopic images were saved in an 8-bit RGB JPEG file format. The stereomicroscopic and DIC images of all sampling times for flasks A and B can be downloaded via the provided link: <https://doi.org/10.14459/2021mp1634565>

2.5 | Determination of the biomass

After taking stereomicroscopic images, the sample was completely transferred into a preweighted Falcon tube and was washed twice with distilled H₂O. The tube was centrifuged after every washing step for 5 min at 10,300 RPM and the supernatant was withdrawn. After 10 h of cultivation, sedimentation replaced the centrifugation steps. The washed biomass within the Falcon tubes was freeze-dried and the dry weight of the biomass was subsequently measured.

2.6 | Determination of glucose concentration in the supernatant

Samples for the determination of glucose concentration were taken every second hour. For that, 1 ml of culture volume was centrifuged and 250 μ l of the supernatant was instantly frozen in liquid nitrogen and stored at -80°C for the subsequent measurement of glucose

concentration. After completing the cultivation, all samples were measured in duplicate using the Glucose GOP/PAP Liquicolor kit (mti-diagnostics GmbH) following the manufacturer's manual.

2.7 | Automated image analysis and data processing

MATLAB (version R2020b; MathWorks) was used to develop a fully automated image analysis pipeline (Figure 1). We discriminated four fungal object classes on the 8-bit stereomicroscopic RGB images. The four object classes are marked on the zoomed sections of the stereomicroscopic images in Figure 2a: (1) nongerminated spores and spore agglomerates (Figure 2a, orange), (2) spore cores comprised of the spore part of germinated spore agglomerates (Figure 2a, red), (3) total pellets composed of spore agglomerate and mycelia (Figure 2a, white), (4) and dispersed mycelia (Figure 2a, green). For better readability, the four classes will be referred to as spores/spore agglomerates, spore cores, pellets, and dispersed mycelia, respectively. Figure 1 shows a flowchart giving an overview of key sections of the developed spore/spore agglomerate, spore core, and pellet segmentation pipeline. In the following, the image analysis steps will be described in detail referring to the subimages labeled a–l in this

visual overview. Images are represented by matrices of intensity values of different color channels. Thus, if matrix operations are performed during image processing, the expression will be used equivalently to the image itself.

2.8 | Segmentation of spores, spore agglomerates, and hyphae of pellets

To binarize spores, spore agglomerates, and spore cores into foreground objects, we used two different threshold methods, that is, the adaptive threshold method and the global threshold method. The adaptive threshold method (Bradley & Roth, 2007) was used for the first 3 h of cultivation to binarize spores and spore agglomerates into foreground objects. The global threshold method, used for images taken after 3 h of cultivation time, was used to binarize spores/spore agglomerates, and spore cores into foreground objects.

For the adaptive threshold method, the 8-bit RGB image was converted into a grayscale image and the function *adaptthresh* (MathWorks) with a sensitivity value of 0.5 was utilized to calculate an adaptive threshold matrix. After thresholding the grayscale image, the black and white values of the binarized image were inverted to obtain the spores and spore agglomerates as foreground objects. An

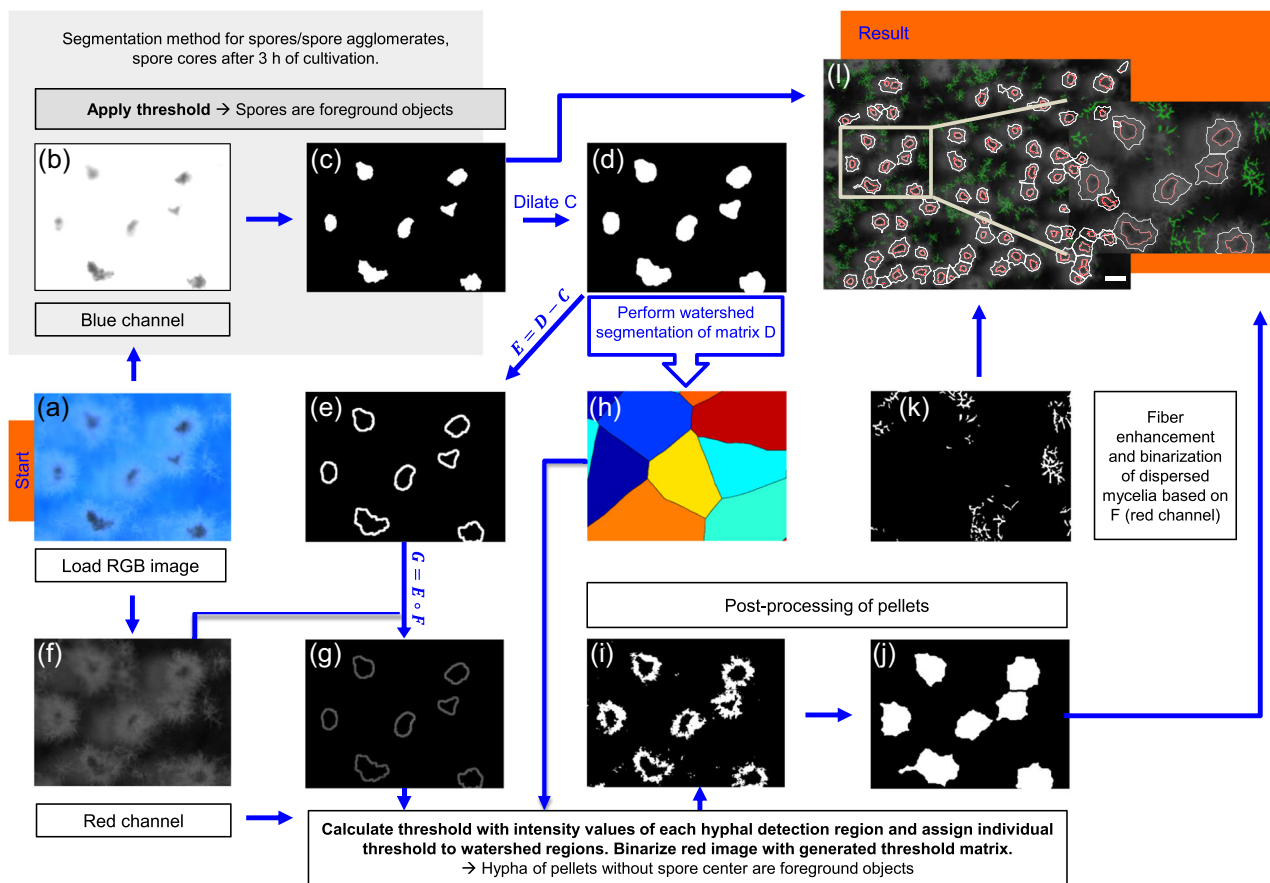


FIGURE 1 Overview of the automated image analysis and data processing resulting in segmentation of spore cores (red), pellets (white), and dispersed mycelium (green) on image I. Images a–k represent a zoomed section of the image I. The scale bar of image I represents a length of 500 μm.

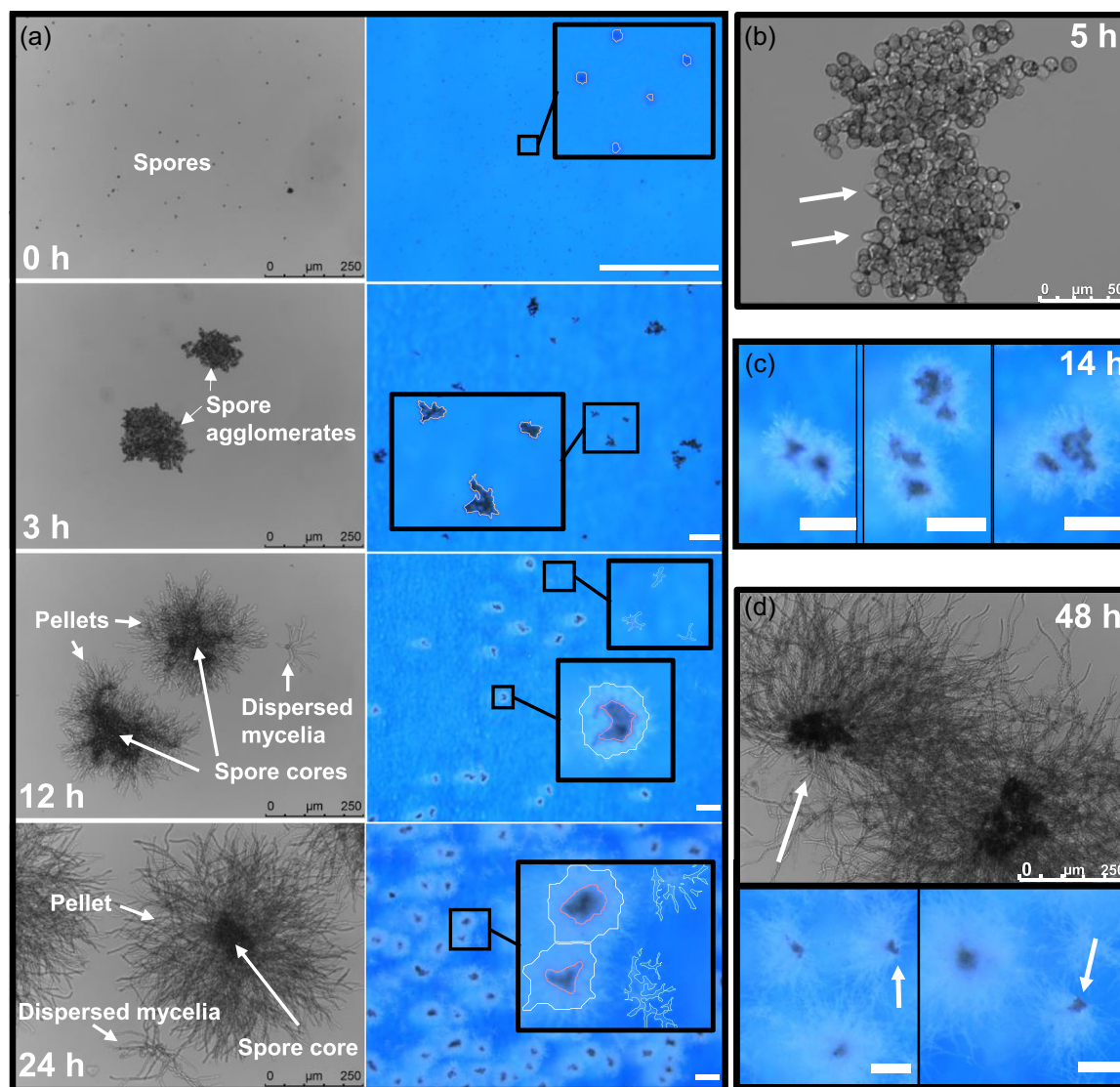


FIGURE 2 Differential interference contrast (DIC) images (grayscale images) and stereomicroscopic images (RGB images) at different cultivation times showing important steps and observations during pellet growth. (a) DIC (left) and stereomicroscopic images (right) with marked spores, spore agglomerates, spore cores, pellets, and dispersed mycelia. The fungal objects to be recognized by the image analysis are indicated on the DIC images (left). The stereomicroscopic images (right) show the fungal objects marked by the image analysis including spores/spore agglomerates (orange) at 0 and 3 h, pellets (white), spore cores (red), and dispersed mycelia (green) at 12 and 24 h of cultivation. The scale bars on the stereomicroscopic images (right) represent a length of 500 μm. (b) DIC image of a spore agglomerate with germinating spores (white arrows) at 5 h of cultivation. (c) Stereomicroscopic images of pellets with multiple spore cores at 14 h of cultivation; the scale bar represents a length of 250 μm. (d) DIC and stereomicroscopic images of broken pellets (white arrows) at 48 h of cultivation; the scale bar represents a length of 250 μm.

illustration of this threshold method can be found in Supporting Information: Figure S2.

For the second segmentation method, the blue channel (Figure 1, subimage b) of the RGB image stack (Figure 1, subimage a) was used for the global threshold method. Blue channel intensity values smaller than 255 were identified as spores and binarized into foreground objects (Figure 1, subimage c). Note that a blue cardboard was used as background for the imaging. In contrast to the black spores, the transparent hyphae of pellets had no blue channel intensity values smaller than 255.

Based on the ongoing agglomeration, the spore agglomerates increased in size. So that a sufficient number of developed spore agglomerates could still be depicted, the magnification was reduced. The change in magnification from a pixel size of 0.82–1.63 μm was chosen to coincide with the switch of the two spore segmentation methods. Spores, spore agglomerates, and spore cores were reliably analyzed with the second spore segmentation method, even in blurred regions. Note that by further using an adaptive threshold, spore cores within pellets would not be sufficiently detected, but the adaptive threshold method showed better performance for the

detection of single spores at early sampling times. However, the initial spore concentration (sampling time 0 h) determined with the image analysis based on stereomicroscopic images differs from the original concentration by a factor of 10 (3.2×10^5 vs. 2.5×10^6 spores/ml) due to a low detection efficiency of single spores in out of focus image regions. Spore agglomerates and spore cores were almost completely detected by the image analysis, which was verified by carefully checking the analyzed stereomicroscope images by visual inspection. Due to the limited spatial resolution, binarized spores and spore agglomerates smaller than an area of 9 pixels were deleted to prevent the false detection of small impurities within the medium and image noise as foreground objects.

Hyphae of pellets were segmented on the red channel image (Figure 1, subimage f). In Figure 1, subimage f, it can be seen that the hyphae have the highest gray intensity values and show a good contrast compared to the background. The general strategy to segment the hyphae is to identify the potential regions of hyphae around each spore agglomerate first and then threshold the red channel intensities within these regions to binarize hyphae into foreground objects. This procedure of calculating a region-dependent threshold enables the detection of hyphae even in blurred image regions. Further, the detection of pellets starts automatically when the red channel intensity values around spore agglomerates reach a certain level, which was adjusted to the intensity values of grown hyphae.

To generate the potential detection regions for hyphae around each spore agglomerate, we dilated the identified spore agglomerates (MATLAB function "imdilate") with a disk-shaped structured element of radius 7 pixels (Figure 1, subimage d) and subtracted the original nondilated spore agglomerate (Figure 1, subimage c), resulting in the ring-shaped binary hyphae detection region (Figure 1, subimage e). By element-wise multiplication of matrix E (Figure 1, subimage e) with the original red channel matrix F (Figure 1, subimage f), the intensity values of the red channel image for each hyphae detection region were obtained (Figure 1, subimage g). The red channel intensity values in subimage g were used to calculate a region-specific threshold T_r for each region around a spore agglomerate. The thickness of the hyphae detection region was chosen to be 7 pixels, as enough red channel intensity values should be used to calculate a representative threshold to binarize all pellets' hyphae into foreground objects. A larger thickness would hinder the detection of short hyphae of young pellets, as pixel intensity values of the background would also be included in the threshold calculation for the short hyphae. Equation (1) was used,

$$T_r = \bar{x}_r - S_r, \quad (1)$$

where \bar{x}_r is the arithmetic mean of the red channel intensity values within a hyphae detection region and S_r is the standard deviation of those intensity values, to calculate the threshold for each region around a spore agglomerate. The regions were defined by performing a watershed segmentation (F. Meyer, 1994) of the Euclidean distance-transformed (Maurer et al., 2003) matrix D (dilated spore agglomerates, Figure 1, subimage d). The threshold values calculated with Equation (1) were assigned to their matching watershed regions

(Figure 1, subimage h), which are defined by the computed watershed lines (Figure 1, subimage h). With this method, a threshold matrix with different thresholds per watershed region was generated, which was used to binarize hyphae on the red channel image into foreground objects (Figure 1, subimage i). The computation of the threshold matrix for the detection of hyphal objects starts from the first sampling times. Regions with calculated threshold values smaller than a red channel intensity value of 60 were set to infinity. Consequently, binarization of pixels into foreground pixels is not possible within those particular threshold regions. Only if the threshold value is greater or equal to 60 will the binarization of pixels into foreground pixels become possible. Although there is some unavoidable arbitrariness involved, the intensity value of 60 was chosen by carefully checking the images and histograms of the images, from which it was concluded that hyphae have significant higher red channel intensity values than 60. After the binarization, the hyphae of pellets were postprocessed.

2.9 | Postprocessing of pellets and detection of spore cores and dispersed mycelia

The postprocessing of the binarized hyphal foreground objects (Figure 1, subimage i) comprises a closing, filling, and image opening step. Thereby, pellet objects were obtained that need to pass a control mechanism to be ultimately recognized as a pellet. To close (MATLAB function "imclose") the fractured hyphal objects (Figure 1, subimage i), a disk-shaped structured element of a radius of 15 pixel was used. To fill the remaining holes in the closed hyphal objects, *imfill* (Matlab function) was used. Thin and elongated protruding structures were removed from the closed and filled hyphal structures by an opening (MATLAB function "imopen") operation with a disk-shaped structured element having a radius of 4 pixels. The resulting matrix was multiplied element-wise with the complement of the binarized watershed line to separate the generated pellet object candidates, grown together during the closing operation. In the last postprocessing step, pellet objects with an equivalent diameter smaller than $25 \mu\text{m}$ were deleted. In a final control step, it was checked if a pellet object was at least connected to one spore agglomerate with an equivalent diameter of $25 \mu\text{m}$ or higher. If not, the object was not identified as a pellet, but had the possibility to be identified as dispersed mycelia. Subimage j in Figure 1 shows the postprocessed binarized pellets. Detected spore agglomerates, which are connected to a pellet, are labeled as spore cores. Figure 1, subimage l displays the original red channel image with marked borders of spore cores (red) and pellets (white).

To identify dispersed mycelia, a vessel enhancement filter (Frangi et al., 1998) was applied to the original red channel image. Since the filter enhances elongated structures and the hyphae of dispersed mycelia are only loosely agglomerated, the vessel enhancement filter (MATLAB function "fibermetric") was capable to increase the intensity values of hyphae belonging to dispersed mycelia. The filtered image was binarized by setting a threshold, which was

calculated with Otsu's method (Otsu, 1979). The result was a binarized image with freely dispersed hyphae as foreground objects (Figure 1, subimage k). Since hyphae of the fluffy outer parts of pellets were also binarized into foreground objects, the calculated pellet objects were deleted from the binarized dispersed mycelia image. A final closing of the dispersed mycelia foreground objects with a square of edge length 3 pixels was performed to connect and smoothen fractured hypha. In Figure 1, subimage l, the binarized image with dispersed mycelia as foreground objects is overlaid in green about the red channel image.

Note that the given image (Figure 1, subimage l) is a sample after 24 h cultivation time. Thus, spores/spore agglomerates without surrounding mycelia are no longer present. Further, dispersed mycelia, spores/spore agglomerates, and pellets touching the image borders were deleted (MATLAB function "imclearborder").

2.10 | Data processing

The four fungal object classes comprising spores/spore agglomerates, spore cores, pellets, and dispersed mycelia were differentiated and analyzed separately on the binarized images. The number of fungal objects and the area-equivalent circular diameter of each object were computed for the class of spores/spore agglomerates, spore cores, and pellets. The area fraction was calculated for all object classes, including dispersed mycelia.

To obtain the analyzed/imaged sample volume for each sampling time, the area fraction under investigation of the Petri dish was multiplied by the original sample volume of 3 ml. The number of analyzed fungal objects on the images per Petri dish was then divided by the analyzed sample volume to obtain the concentration of spore/spore agglomerates, spore cores, and pellets.

To create the cumulative size distributions $Q_0(d) = \int_0^d q_0(d')dd'$ of spores/spore agglomerates, spore cores, and pellets per sampling time, the values of the area-equivalent circular diameter d, d' were divided into 15 equidistant size classes between the minimal and maximal fungal object diameter. q_0 is the normalized number density distribution. While d is the argument of the cumulative distribution function, d' is the integration variable. To assess the change in the distributions over the cultivation time, the same grid of the size data for all sampling times was applied. Since objects touching the image border were deleted, a bias would be introduced in the size distributions as large objects are more likely to touch the image border than smaller ones. Thereby, the proportion of large objects would be underestimated in comparison to smaller objects. To consider this bias, the correction factor

$$CF_{\text{class}} = \frac{h_{\text{image}} \times w_{\text{image}}}{(h_{\text{image}} - d_{\text{class_mid}}) \times (w_{\text{image}} - d_{\text{class_mid}})} \quad (2)$$

was introduced for each class, where h_{image} and w_{image} indicate the image height and width. The correction factor increases with the size of $d_{\text{class_mid}}$, which is the diameter of the midpoint per class. The introduced correction factor is based on the "adjusted count"

method, which is described in Russ (2016). CF_{class} was multiplied with each class of the number density distributions $q_0(d)$.

In addition, box-and-whisker plots were used to describe the distributions of the equivalent diameter of spores/spore agglomerates during cultivation. The whiskers and the outliers of the box-and-whisker plots were calculated by 1.5 times the interquartile range.

The area fraction of each object class was calculated by the ratio between the sum of object areas within the class and the total area of all captured images per sampling time.

To evaluate the locations of spore cores within pellets and to observe asymmetric positions of the spore cores relating to the pellet center, we calculated the Euclidean distance between the coordinates of the centroid of a pellet and the centroid of its spore core. This calculation was performed for pellets containing only one spore core. The obtained data were used to calculate cumulative distributions of the Euclidean distances at different sampling times.

3 | RESULTS AND DISCUSSION

In this study, we demonstrate the potential of a newly developed image analysis pipeline (Figure 1) to investigate the morphological development of a filamentous fungal culture into pellets and dispersed mycelia and to describe population heterogeneities. Exemplarily, we present data for duplicate *A. niger* batch cultivations performed in shake flasks for 48 h. Examples of DIC and stereomicroscopic images at all sampling times for cultivation flask A are shown in Supporting Information: Figure S3. With the developed image analysis pipeline (see Figure 1 and Section 2), we were able to analyze both spore agglomeration and growth of *A. niger* pellets during submerged cultivation. At 44 sampling times, about 42,700 spores/spore agglomerates, 35,500 spore cores, and 33,000 pellets were analyzed in total for culture flask A, and 66,300, 34,000, and 31,500, respectively, for the duplicate culture flask B. The lowest numbers of analyzed objects per class and sampling time were 600 for flask A and 400 for flask B, respectively.

3.1 | Overall cultural development

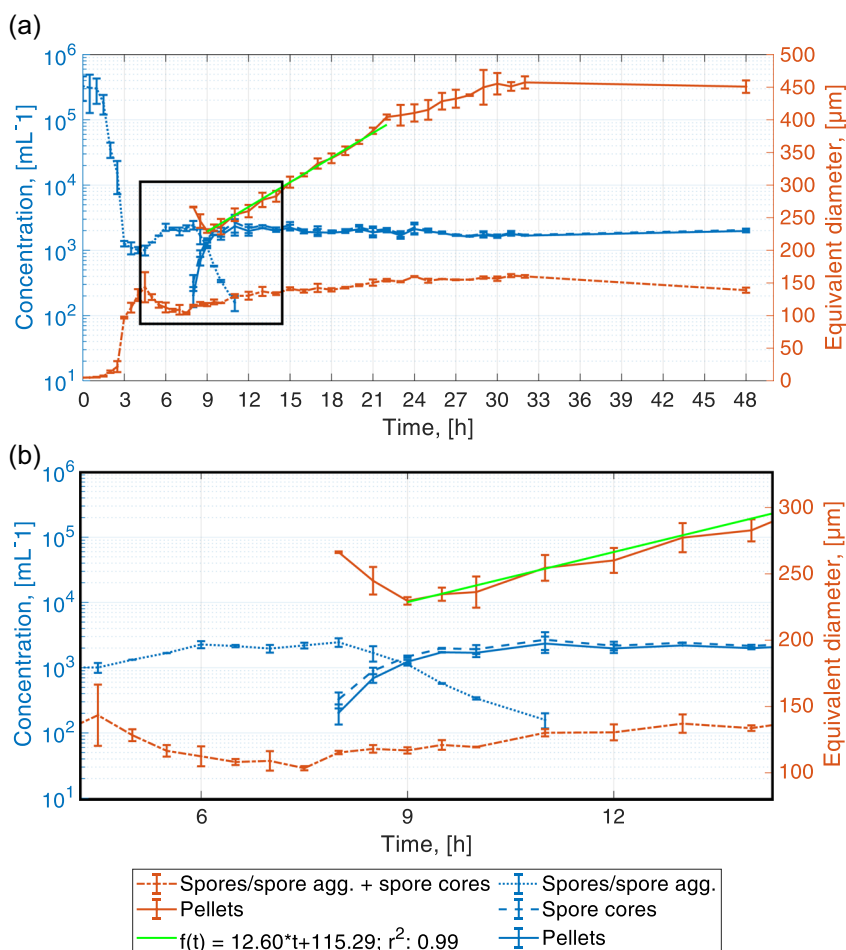
Figure 3 provides an overview focusing on spore agglomeration and pellet growth with calculated mean concentrations (left ordinate) and mean equivalent diameters of the fungal objects (right ordinate) per cultivation flask over time (abscissa). Small standard deviations between both duplicates demonstrate high reproducibility of the cultivation method and the developed image analysis pipeline. As depicted in Figure 3a, spore concentration decreases starting from 1 until 4.5 h and the equivalent diameter of spores/spore agglomerates increases. This indicates that spore agglomeration already starts after 1 h, forming spore agglomerates with a mean equivalent diameter of about 140 µm at 4.5 h. This observation agrees with the qualitative analysis of the DIC images. Selected examples of DIC and stereomicroscope images for all sampling times for flask A can be found in the Supporting Information: Figure S3. Exemplary spore agglomerates at 3 h are shown in Figure 2a. Surprisingly,

from 4.5 h on, spore/spore agglomerate concentrations increase and spore agglomerate equivalent diameters decrease, indicating breakage of spore agglomerates possibly due to the start of germination (Figure 3a). Figure 2b shows germinating spores of a spore agglomerate at 5 h. After 6 h, the concentration of spores/spore agglomerates remains almost constant until the first pellets become detected at 8 h (Figure 3b). The first pellets are detected at a sampling time of 8 h and not from the start of germination at 5 h, as a certain length of hyphae is needed to calculate a pellet specific threshold with the method described in the image analysis section (see Section 2). Consequently, the concentration of spore agglomerates decreases only from 8 h and not at earlier sampling times, which might be expected from a biological point of view. At 8 h, the difference between the mean equivalent diameter of pellets (266 μm) and spore agglomerates (115 μm) is about 150 μm (Figure 3b), due to the thickness of the hyphal layer around the spore agglomerates needed for pellet detection. Further, pellets with large spore agglomerates are detected first in comparison to smaller pellets, resulting in an overestimation of the mean value for the whole population. At 9 h, the growth of hyphae enables the detection of smaller pellets as well, resulting in an increased pellet concentration and a decreased mean equivalent pellet diameter of 228 μm . At 12 h, all spore agglomerates grew into spore cores within pellets. The concentration of spore cores of pellets after 12 h is nearly similar to the spore agglomerate concentration after 6 h (Figure 3b). Therefore, we calculated the mean number of spores per

pellet with the ratio of the initial spore concentration in the medium of 2.5×10^6 spores/ml and the concentration of pellets at 12 h (1975 pellets/ml), resulting in about 1265 spores per pellet, assuming that all spores have agglomerated and all spore agglomerates have built a pellet. Notably, the concentration of spore cores is slightly higher than the concentration of pellets (Figure 3b), as pellets can contain multiple spore cores as shown in Figure 2c. At 12 h, a pellet contains an average of about 1.1 spore cores. From 9 to 22 h, a constant growth rate of 12.6 $\mu\text{m}/\text{h}$ of the pellet mean equivalent diameter was calculated with a simple linear regression model with a coefficient of determination of 0.99 (Figure 3a).

Figure 4 shows the development of the mean glucose and biomass concentration for flasks A and B (right ordinate) and the area fraction of the fungal structures (left ordinate), which is the sum of the area fractions of nongerminated spores/spore agglomerates, pellets (including spore cores), and dispersed mycelia. The development of the area fraction of the fungal structures shows the same trend as the development of the determined biomass concentration per sampling time, except for the values at 30 and 31 h. We strongly assume measurement errors for the biomass concentrations at the sampling times of 30 and 31 h. The glucose concentration constantly decreases from 10 to 32 h and behaves as expected, inversely proportional to the area fraction of the fungal structures and the accumulated biomass. The slower increase in biomass and the area fraction between 32 and 48 h indicates the end of the exponential growth phase due to glucose limitation.

FIGURE 3 Overview on spore agglomeration and pellet growth with calculated mean number concentrations and mean equivalent diameters of spores/spore agglomerates, spore cores, and pellets per sampling time. (a) The graphs were calculated with the data obtained by the image analysis of the stereo microscope images. The shown data of number concentrations (left ordinate) and equivalent diameters (right ordinate) are mean values, calculated with the mean of flasks A and B. Spores/spore agglomerates (spore agg.) indicate ungerminated spores and spore agglomerates. Spore cores are detected spore agglomerates within pellets. The error bars indicate the standard deviation between the mean of flasks A and B. The function $f(t)$ was calculated by a linear regression model. The slope of 12.60 $\mu\text{m}/\text{h}$ indicates the growth velocity of the pellet equivalent diameter from 9 to 22 h. (b) Zoomed section of the rectangle in (a).



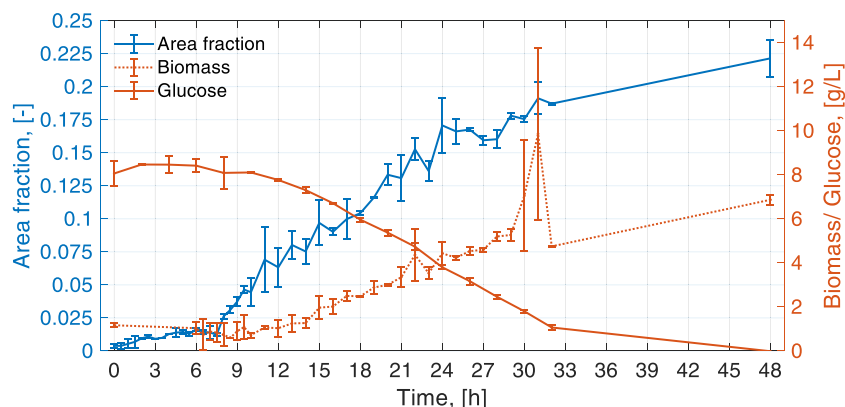


FIGURE 4 Total area fractions of the fungal structures (left ordinate, blue) as well as biomass and glucose concentration (right ordinate, orange) for all 44 sampling times. The total area fraction of the fungal structures is the sum of the area fractions of spores, spore agglomerates, pellets (including spore cores), and dispersed mycelia. The data of the area fractions were determined by the image analysis based on stereomicroscopic images. The depicted area fractions are mean values, calculated with the total area fractions for flasks A and B. The error bars indicate the standard deviation between flasks A and B. The orange gridlines and the right ordinate show the mean biomass (dotted line) and glucose (solid line) concentration in the medium of flasks A and B per sampling time.

Figure 5 displays the area fractions of all fungal objects. The area fraction of dispersed mycelia constantly increases from 7.5 to 32 h and shows reduced growth from 32 h. Due to the loose structure of dispersed mycelia, we assume that nutrient and oxygen transfer limitation from the medium bulk phase to the hyphae is a minor factor, but that glucose limitation is the main reason for the growth limitation of dispersed mycelia. The slower increase of the area fraction of pellets starts already from 24 h. In addition, the area fraction (Figure 5) and the equivalent diameter (Figure 3a) of spore cores do not increase anymore from 24 h.

Assuming that the growth of hyphae within spore cores enlarges the spore core, growth limitations due to transfer hindrance of nutrients and oxygen through the dense hyphal pellet structure could be a reason for the stagnating area fraction of spore cores. At 24 h, a pellet mean equivalent diameter of 410 μm can be observed (Figure 3a). Driouch et al. (2012) and Hille et al. (2009) proposed a critical diameter of 400 μm at which oxygen transfer limitations can occur within *A. niger* pellets. Here, it must be mentioned that a critical diameter for oxygen transfer limitations depends on the hyphal density within a pellet (Schmieder et al., 2019, 2020).

The area fraction of spores and spore agglomerates slightly increases until 6 h (Figure 5). The isotropic swelling of spores results in higher area fraction values of spores and spore agglomerates, as the diameter of *Aspergillus* spores increases twofold or more before germination (Van Leeuwen et al., 2013). Further, spore agglomerates, which are built by the agglomeration between spore agglomerates, enclose hollow regions resulting in an overestimation of the area fraction of spore agglomerates.

3.2 | Spore agglomeration

The high amount of analyzed fungal objects per sampling time made it possible to calculate size distributions. To represent the evolution

of the distributed size of spores/spore agglomerates, spore cores, and pellets throughout cultivation, we used the cumulative size distribution $Q_0(d)$. Figure 6 exemplarily depicts the time evolution of $Q_0(d)$ of spores/spore agglomerates and spore cores for flask A. The distribution evolution for flask B can be found in Supporting Information: Figure S4. The boxplots in Figure 7 summarize the distributions of all equivalent diameters of spores/spore agglomerates and spore cores per sampling time for flask A. The boxplots per sampling time for flask B can be found in the Supporting Information: Figure S5.

In Figure 6, it can be observed that the d_{90} value at 0 h of the cumulative size distribution is about 6.6 μm , which means that 90% of all analyzed spores of flask A at 0 h (start of cultivation) have an equivalent diameter less or equal to about 6.6 μm . This indicates that the spores are individually dispersed. Manually measured diameters of 37 single spores on the DIC images at 0 h range between 4 and 7.6 μm with a mean of 5.3 μm and a standard deviation of 0.6 μm . At 2 h, the equivalent diameter of 90% of spores and spore agglomerates is shifted to less or equal to about 28 μm (d_{90} value). Large spore agglomerates already reach a size of about 190 μm . The shift of the distributions from a convex to a concave curvature at 3 h shows the increase of the equivalent diameter for all size classes and the rise of the spore agglomeration. The cumulative size distributions at 4.5 h indicate a d_{90} value of spore agglomerates of 253 μm . Larger agglomerates may form by agglomeration of already formed agglomerates. The comparison of the distributions of 4.5 and 6 h suggests that such large spore agglomerates (>200 μm) at 4.5 h break into smaller spore agglomerates at 6 h, as growing hyphae due to the start of germination between 4.5 and 6 h lead to the mechanical separation of loose connections between spore agglomerates. At 6 h, the d_{90} value decreases to about 220 μm . At 8 h, the first pellets and thus spore cores are detected. The cumulative size distribution (Figure 6) and the boxplot (Figure 7) at 8 h indicate that 50% of the

FIGURE 5 Mean area fractions for fungal objects per sampling time. The mean area fractions are calculated with the area fractions for flasks A and B. The error bars indicate the standard deviation between flasks A and B. The data of the area fractions were determined by the image analysis based on stereomicroscopic images. Spore cores are detected spore agglomerates within pellets.

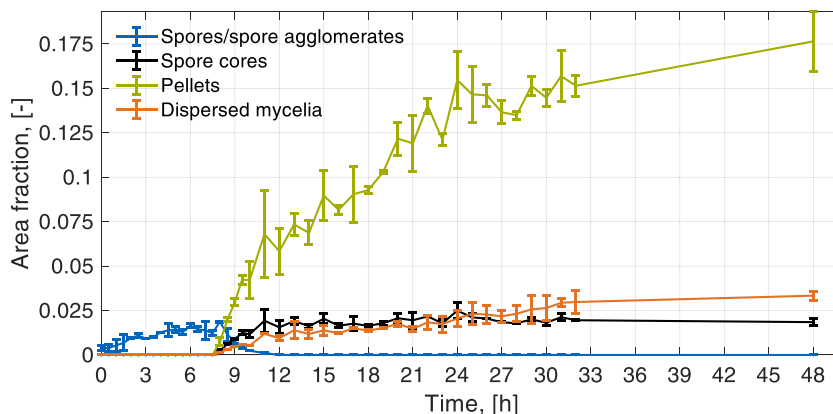


FIGURE 6 Cumulative size distributions $Q_0(d)$ of equivalent diameters of spores, spore agglomerates, and spore cores of flask A at different sampling times. The data were determined by the image analysis based on stereomicroscopic images. The dashed lines indicate the d_{90} values.

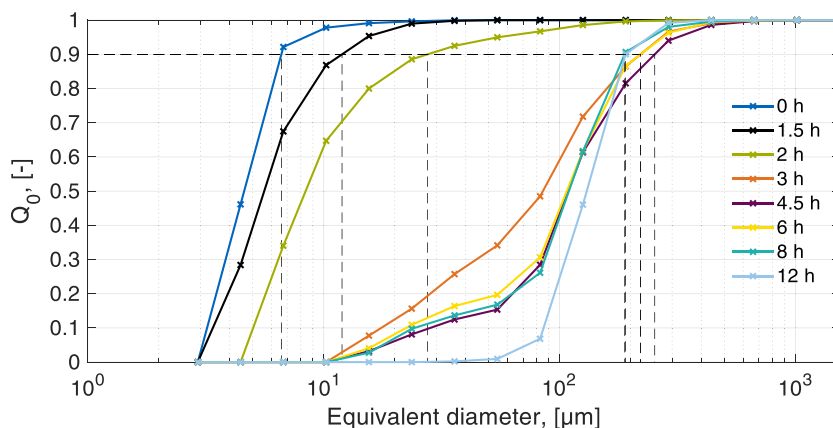
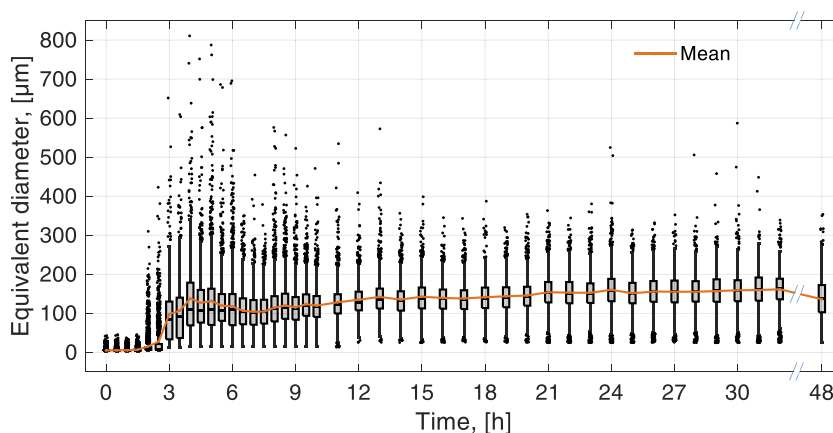


FIGURE 7 Boxplots of equivalent diameters of spores, spore agglomerates, and spore cores per sampling time for flask A. Black lines within the boxes mark the median. The outliers are indicated by scattered black dots. The orange graph shows the mean equivalent diameter of all detected spores, spore agglomerates, and spore cores per sampling time. The data were determined by the image analysis based on stereomicroscopic images.



equivalent diameters of spore agglomerates and spore cores range between 70 and 140 μm . The cumulative size distribution at 12 h, when no spore agglomerates without hyphae are detected anymore, shows an increase in the equivalent diameter of spore cores (Figure 6). As stated above, this observation possibly goes along with the growth of hyphae in the center of spore cores, resulting in an increased equivalent diameter of detected spore cores. The boxplots in Figure 7 furthermore indicate that the highest heterogeneity can be observed during the first 9 h after inoculation. Also, it demonstrates that the spore core equivalent diameters further increase between 12 and 24 h due to the shift of the boxes,

representing the middle 50% of the data, to larger equivalent diameters. The median and the mean increase from about 130 μm at 12 h to 160 μm at 24 h. From 24 to 32 h, that is, when glucose becomes limited, the increase of the spore cores stagnates and 50% of the equivalent diameters remain constant between 130 and 190 μm . It has previously been shown that glucose limitation, and thus the onset of starvation, leads to autophagic processes in *A. niger* to recycle carbon intracellularly (Nitsche et al., 2012, 2013). Compared to 32 h, the distribution of 48 h shows a decrease in the equivalent diameters of spore cores. At 48 h, 50% of equivalent diameters range between 100 and 170 μm . The median and the mean

decrease to about 135 μm . Due to the decreased equivalent diameters and the increased concentration of spore cores at 48 h compared to 32 h in Figure 3a, we assume pellet breakage at the spore core. We will further discuss this hypothesis by taking the cumulative size distributions $Q_0(d)$ of the pellet equivalent diameters into account.

3.3 | Pellet growth and breakage

The growth and structural development of pellets within the cultivation can be tracked with the cumulative size distributions $Q_0(d)$ of the equivalent diameter of pellets per sampling time. Figure 8 displays the cumulative size distributions $Q_0(d)$ of flask A. The normalized number density distributions $q_0(d)$ of flask A at different sampling times are shown in the Supporting Information: Figure S6. In addition, the cumulative size distributions $Q_0(d)$ and the normalized number density distributions $q_0(d)$ of flask B can be found in the Supporting Information: Figures S7 and S8. Further, the boxplots of equivalent diameters of pellets per sampling time can be found in the Supporting Information: Figures S9 and S10. The shift of the cumulative distributions of flask A (Figure 8) and flask B (Figure S7) to larger diameters until the sampling time of 32 h indicates the growth of pellets of all size classes. From sampling times from 24 until 48 h, the cumulative size distributions of flasks A and B become wider, showing an increase in the heterogeneity of the pellet size probably due to breakage and agglomeration events of hyphal structures. This can also be seen in the normalized number density distributions $q_0(d)$ of flasks A and B in the Supporting Information: Figures S6 and S8. By comparing the sampling times at 32 and 48 h, the size distribution of flask A at 48 h shows a larger number of pellets within the equivalent diameter range from about 200 and 390 μm and a lower number of pellets with an equivalent diameter between 390 and 510 μm (Figure 8 and Supporting Information: Figure S6). Supporting Information: Figures S7 and S8 show a similar observation for flask B. Figure 3a also shows a decrease in the pellet mean equivalent diameter and an increase in the pellet concentration from 32 to 48 h. Note that a pellet can break into two new pellets, which are detected by the image analysis, leading to an increased pellet number concentration. Although the mean equivalent diameter of pellets in Figure 3a stagnates from 30 h or even slightly

decreases from 32 h, the area fraction of pellets in Figure 5 further increases between 32 and 48 h. These observations lead to the hypothesis that pellets grow to a certain size until increasing shear forces act upon them. Also, inactive cells due to oxygen and glucose limitations in central parts result in weaker bonding forces between the cells and finally in pellet break up (Figure 2d). Glucose limitation and eventually starvation are explained by dramatic transcriptomic changes, as about 7000 out of the 14,000 genes of *A. niger* become differentially expressed in the postexponential growth phase compared to the exponential growth phase (Nitsche et al., 2012). Among those are genes encoding for secreted hydrolytic enzymes including chitinases, glucanases, proteases, and phospholipases that remodel (and supposedly weaken) the cell surface of *A. niger*. Pellet fragmentation leading to increased population heterogeneity can also be induced by a change of the carbon source from glucose to maltose (Tegelaar et al., 2020). This could potentially be caused by a short period of carbon limitation. Posch et al. (2012) assumed pellet breakage due to oxygen transfer limitation to the pellet core at area-equivalent circular diameters between 350 and 400 μm . Hille et al. (2009) stated that above a critical pellet diameter of about 400 μm , diffusion limitation in the pellet core of *A. niger* occurs. Driouch et al. (2012) verified this critical radius with the use of a green fluorescent protein producing *A. niger* strain. In Figure 8, the d_{50} value of the cumulative size distribution at 24 h of flask A shows that 50% of the analyzed pellets have equivalent diameters larger than a diameter of 400 μm . At 32 h, the d_{50} value even increases to about 450 μm , leading to the assumption of oxygen and nutrient limitation followed by pellet breakage at the pellet center within 48 h of cultivation.

As already mentioned, Figures 3a and 7 show a smaller mean equivalent diameter of spore cores at 48 h compared to 32 h. These observations lead to the hypothesis that pellet breakage occurs at the spore core of a pellet, which is normally located in the center of a pellet. Figure 2d shows a DIC image of a pellet, which has broken at its spore core and two exemplary stereomicroscopic images with broken pellets at 48 h of cultivation. Buffo et al. (2020) observed the breakage of pellets into large pellet fragments with sizes between 200 and 500 μm during *A. niger* bioreactor cultivations. Pictures in their publication show these fragments breaking out of central pellet parts.

To statistically strengthen the hypothesis that breakage through the central parts of the pellets occur, we used the distance between the

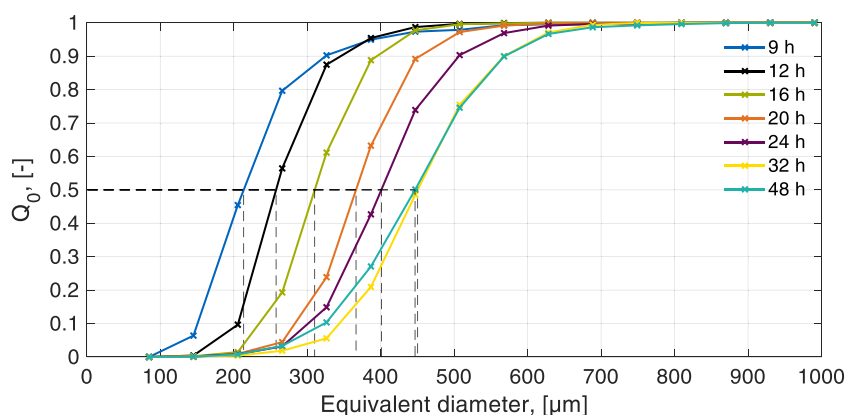


FIGURE 8 Cumulative size distributions $Q_0(d)$ of the equivalent diameters of pellets at different sampling times for flask A. The data were determined by the image analysis based on stereomicroscopic images. The dashed lines indicate the d_{50} values.

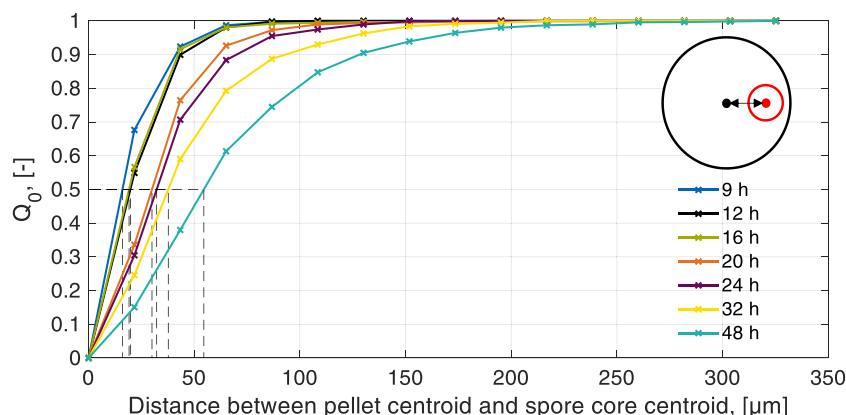


FIGURE 9 Cumulative distribution of Euclidean distances between the centroid of the pellet and the centroid of the spore core at different sampling times for flask A. The schematic drawing in the upper right corner depicts the distance between the pellet centroid (black dot) and the spore core centroid (red dot). The data were determined by the image analysis based on stereomicroscopic images. The dashed lines indicate the d_{50} values. The distances were calculated for pellets containing one spore core.

centroid of the pellet and the centroid of the pellets' spore core as a measure of the eccentricity. Such measure is directly linked to the asymmetry of a pellet and increasing asymmetry should be expected if central breakage of pellets occurs. Figure 9 shows the cumulative distribution of the distance between the centroid of the pellet and the centroid of the pellets' spore core for all pellets per sampling time for flask A. The same graph for flask B can be found in the Supporting Information: Figure S11. Note that we calculated the distance between the centroids for pellets that contain only one spore core. However, starting from sampling time 12 h, over 91% of the pellets per sampling time of flasks A and B contained only one spore core. A "perfect" spherical pellet with a spherical spore core in the pellet center would have a distance of zero. The increase of the d_{50} values indicates an increasing asymmetry of the position of the spore cores within pellets. Reasons for this observation could be the agglomeration of dispersed mycelia and pellets, or breakage of hyphae due to shear forces and asymmetric growth of the pellet. Since almost no increase of the equivalent diameters of pellets starting from about 390 μm can be observed between 32 and 48 h in Figure 8 and Supporting Information: Figure S7, we assume that breakage of pellets results in the increased centroid distances between 32 and 48 h in Figure 9. Therefore, the increase of the centroid distance between 32 and 48 h provides additional evidence of pellet breakage at its spore core since the spore core is no longer in the middle of a pellet due to the breakage.

4 | CONCLUSION

The present study describes a new high-throughput image analysis pipeline based on stereomicroscopic images. The new method has a considerable advantage over already existing tools in that it can track both the spore agglomeration and the structural development of pellets during growth. This added value in comparison to other image analysis tools, for example, SPARTICLE by Willemse et al. (2018), is realized by detecting multiple fungal object classes at ones without additional user

input. Within a stereomicroscopic image, spores/spore agglomerates, pellets, spore cores, which are spore agglomerates within pellets, and dispersed mycelia can be segmented and analyzed. Our image analysis is computationally undemanding. Thus, the developed algorithm can analyze 30 images that only contain spores within one minute with a standard desktop PC (AMD Ryzen 7 2700 Eight-Core Processor; 3.4 GHz); 30 images that also show pellets can be calculated within 4 min. The image capturing of 30 images including the sampling could be performed within 10 min. Regarding the short image capturing and processing time, the new method can provide information and conclusions about the development during cultivation.

The proposed method can quantify the morphological evolution during the cultivation of filamentous fungal pellets. Starting from the inoculum, the spore agglomeration, transitioning to hyphal growth, and the macromorphological development of pellets as well as the amount of dispersed mycelia can be tracked. Thus, our method enables one to study the influence of cultivation conditions, including, for example, medium composition, inoculum concentration, pH, temperature, agitation, aeration, or microparticles as well as the impact of genetic modifications on the spore agglomeration but also on the pellet morphology during cultivation. Based on *A. niger* cultivations of 48 h, we demonstrated the potential of the developed image analysis. With the calculated spore and spore agglomerate size distributions of different time steps during cultivation, we could observe the breakage of large spore agglomerates (>200 μm) into smaller ones from the beginning of germination. Based on the quantification of spore cores, the size distributions of pellets, together with the area fractions, and physiological data (glucose consumption, and biomass formation), a hypothesis about pellet breakage at the spore core has been corroborated as a consequence of mass transfer limitations in the interior of pellets. A wider pellet size distribution at the end of the cultivation run, possibly caused by pellet breakage, indicated an increased cultural heterogeneity. Summarizing, the combination of high-throughput, tracking of both spore agglomeration and pellet development, as well as the automated detection of spores,

spore agglomerates, spore cores, and pellets at different sampling times within one computation run, renders the proposed image analysis a valuable tool for studying the morphological development of filamentous fungal pellets during cultivation.

ACKNOWLEDGMENTS

The authors thank Nadine Münch and Florian Edenhofner for preliminary studies on image analysis and data processing. We also wish to thank Ali Khajehesamedini and Tiaan Friedrich for helpful and fruitful discussions. The authors thank the Deutsche Forschungsgemeinschaft for financial support for this study within the SPP 1934 DiSPBiotech—315384307 and 315305620 and SPP2170 InterZell—427889137. Open access funding was enabled and organized by Projekt DEAL.

CONFLICTS OF INTEREST

The authors declare no conflicts of interest.

DATA AVAILABILITY STATEMENT

The data that support the findings of this study are available from the corresponding author upon reasonable request. Data and image analysis scripts are available for readers upon request.

ORCID

Henri Müller  <http://orcid.org/0000-0002-4831-0003>

Lars Barthel  <http://orcid.org/0000-0001-8951-5614>

Stefan Schmideder  <http://orcid.org/0000-0003-4328-9724>

Tabea Schütze  <http://orcid.org/0000-0001-7630-3794>

Vera Meyer  <http://orcid.org/0000-0002-2298-2258>

Heiko Briesen  <http://orcid.org/0000-0001-7725-5907>

REFERENCES

- Bekker, C., de van Veluw, G. J., Vinck, A., Wiebenga, L. A., & Wösten, H. A. B. (2011). Heterogeneity of *Aspergillus niger* microcolonies in liquid shaken cultures. *Applied and Environmental Microbiology*, 77(4), 1263–1267. <https://doi.org/10.1128/AEM.02134-10>
- Bennet, J. W., & Lasure, L. L. (1991). *More gene manipulations in fungi*. Academic Press
- Böl, M., Schrinner, K., Tesche, S., & Krull, R. (2021). Challenges of influencing cellular morphology by morphology engineering techniques and mechanical induced stress on filamentous pellet systems—A critical review. *Engineering in Life Sciences*, 21(3–4), 51–67. <https://doi.org/10.1002/elsc.202000060>
- Bradley, D., & Roth, G. (2007). Adaptive thresholding using the integral image. *Journal of Graphics Tools*, 12(2), 13–21. <https://doi.org/10.1080/2151237X.2007.10129236>
- Buffo, M. M., Esperança, M. N., Farinas, C. S., & Badino, A. C. (2020). Relation between pellet fragmentation kinetics and cellulolytic enzymes production by *Aspergillus niger* in conventional bioreactor with different impellers. *Enzyme and Microbial Technology*, 139, 109587. <https://doi.org/10.1016/j.enzmictec.2020.109587>
- Cairns, T. C., Feurstein, C., Zheng, X., Zheng, P., Sun, J., & Meyer, V. (2019). A quantitative image analysis pipeline for the characterization of filamentous fungal morphologies as a tool to uncover targets for morphology engineering: A case study using apID in *Aspergillus niger*. *Biotechnology for Biofuels*, 12, 149. <https://doi.org/10.1186/s13068-019-1473-0>
- Cairns, T. C., Nai, C., & Meyer, V. (2018). How a fungus shapes biotechnology: 100 years of *Aspergillus niger* research. *Fungal Biology and Biotechnology*, 5, 13. <https://doi.org/10.1186/s40694-018-0054-5>
- Cairns, T. C., Zheng, X., Zheng, P., Sun, J., & Meyer, V. (2019). Moulding the mould: Understanding and reprogramming filamentous fungal growth and morphogenesis for next generation cell factories. *Biotechnology for Biofuels*, 12, 77. <https://doi.org/10.1186/s13068-019-1400-4>
- Commer, B., & Shaw, B. D. (2020). Current views on endocytosis in filamentous fungi. *Mycology*, 12(1), 1–9. <https://doi.org/10.1080/21501203.2020.1741471>
- Cox, P. W., Paul, G. C., & Thomas, C. R. (1998). Image analysis of the morphology of filamentous micro-organisms. *Microbiology*, 144(4), 817–827.
- Drriouch, H., Haensch, R., Wucherpfennig, T., Krull, R., & Wittmann, C. (2012). Improved enzyme production by bio-pellets of *Aspergillus niger*: Targeted morphology engineering using titanate microparticles. *Biotechnology and Bioengineering*, 109(2), 462–471.
- Drriouch, H., Sommer, B., & Wittmann, C. (2010). Morphology engineering of *Aspergillus niger* for improved enzyme production. *Biotechnology and Bioengineering*, 105(6), 1058–1068.
- Dynesen, J., & Nielsen, J. (2003). Surface hydrophobicity of *Aspergillus nidulans* conidiospores and its role in pellet formation. *Biotechnology Progress*, 19(3), 1049–1052. <https://doi.org/10.1021/bp0340032>
- Ehgartner, D., Herwig, C., & Fricke, J. (2017). Morphological analysis of the filamentous fungus *Penicillium chrysogenum* using flow cytometry—The fast alternative to microscopic image analysis. *Applied Microbiology and Biotechnology*, 101(20), 7675–7688.
- Fiedler, M. R. M., Barthel, L., Kubisch, C., Nai, C., & Meyer, V. (2018). Construction of an improved *Aspergillus niger* platform for enhanced glucoamylase secretion. *Microbial Cell Factories*, 17, 17.
- Fiedler, M. R. M., Cairns, T. C., Koch, O., Kubisch, C., & Meyer, V. (2018). Conditional expression of the small GTPase ArfA impacts secretion, morphology, growth, and actin ring position in *Aspergillus niger*. *Frontiers in Microbiology*, 9, 878. <https://doi.org/10.3389/fmicb.2018.00878>
- Frangi, A. F., Niessen, W. J., Vincken, K. L., & Viergever, M. A. (1998). Multiscale vessel enhancement filtering. In W. M. Wells, A. Colchester, & S. Delp (Eds.), *Lecture notes in computer science: Vol. 1496. Medical Image Computing and Computer-Assisted Intervention—MICCAI'98: First International Conference Cambridge, MA, USA, October 11–13, 1998 Proceedings* (pp. 130–137). Springer. <https://doi.org/10.1007/BFb0056195>
- Gibbs, P. A., Seviour, R. J., & Schmid, F. (2000). Growth of filamentous fungi in submerged culture: Problems and possible solutions. *Critical Reviews in Biotechnology*, 20(1), 17–48.
- Grimm, L. H., Kelly, S., Hengstler, J., Gobel, A., Krull, R., & Hempel, D. C. (2004). Kinetic studies on the aggregation of *Aspergillus niger* conidia. *Biotechnology and Bioengineering*, 87(2), 213–218.
- Hille, A., Neu, T. R., Hempel, D. C., & Horn, H. (2009). Effective diffusivities and mass fluxes in fungal biopellets. *Biotechnology and Bioengineering*, 103(6), 1202–1213.
- Kaup, J.-A., Ehrlich, K., Pescheck, M., & Schrader, J. (2008). Microparticle-enhanced cultivation of filamentous microorganisms: Increased chloroperoxidase formation by *Caldariomyces fumago* as an example. *Biotechnology and Bioengineering*, 99(3), 491–498.
- Kurt, T., Marbà-Ardébol, A.-M., Turan, Z., Neubauer, P., Junne, S., & Meyer, V. (2018). Rocking *Aspergillus*: Morphology-controlled cultivation of *Aspergillus niger* in a wave-mixed bioreactor for the production of secondary metabolites. *Microbial Cell Factories*, 17(1), 128. <https://doi.org/10.1186/s12934-018-0975-y>
- Kwon, M. J., Nitsche, B. M., Arentshorst, M., Jorgensen, T. R., Ram, A. F. J., & Meyer, V. (2013). The transcriptomic signature of RacA activation and inactivation provides new insights into the morphogenetic network of *Aspergillus niger*. *PLoS One*, 8(7), 68946.

- Laible, A. R., Dinius, A., Schrader, M., Krull, R., Kwade, A., Briesen, H., & Schmideder, S. (2021). Effects and interactions of metal oxides in microparticle-enhanced cultivation of filamentous fungi and bacteria. *Engineering in Life Sciences*. Advance online publication. <https://doi.org/10.1002/elsc.202100075>
- Maurer, C. R., Qi, R., & Raghavan, V. (2003). A linear time algorithm for computing exact Euclidean distance transforms of binary images in arbitrary dimensions. *IEEE Transactions on Pattern Analysis and Machine Intelligence*, 25(2), 265–270. <https://doi.org/10.1109/TPAMI.2003.1177156>
- Meyer, F. (1994). Topographic distance and watershed lines. *Signal Processing*, 38(1), 113–125. [https://doi.org/10.1016/0165-1684\(94\)90060-4](https://doi.org/10.1016/0165-1684(94)90060-4)
- Meyer, V., Basenko, E. Y., Benz, J. P., Braus, G. H., Caddick, M. X., Csukai, M., de Vries, R. P., Endy, D., Frisvad, J. C., Gunde-Cimerman, N., Haarmann, T., Hadar, Y., Hansen, K., Johnson, R. I., Keller, N. P., Kraševac, N., Mortensen, U. H., Perez, R., Ram, A., ... Wösten, H. (2020). Growing a circular economy with fungal biotechnology: A white paper. *Fungal Biology and Biotechnology*, 7(1), 5. <https://doi.org/10.1186/s40694-020-00095-z>
- Meyer, V., Ram, A. F. J., & Punt, P. J. (2010). Genetics, genetic manipulation, and approaches to strain improvement of filamentous fungi. In R. H. Baltz, J. E. Davies, & A. L. Demain (Eds.), *Manual of industrial microbiology and biotechnology* (3rd ed., pp. 318–329). ASM Press. <https://doi.org/10.1128/9781555816827.ch22>
- Miyazawa, K., Yoshimi, A., & Abe, K. (2020). The mechanisms of hyphal pellet formation mediated by polysaccharides, α -1,3-glucan and galactosaminogalactan, in *Aspergillus* species. *Fungal Biology and Biotechnology*, 7(1), 10. <https://doi.org/10.1186/s40694-020-00101-4>
- Nepal, K. K., & Wang, G. (2019). Streptomycetes: Surrogate hosts for the genetic manipulation of biosynthetic gene clusters and production of natural products. *Biotechnology Advances*, 37(1), 1–20. <https://doi.org/10.1016/j.biotechadv.2018.10.003>
- Nitsche, B. M., Burggraaf-van Welzen, A.-M., Lamers, G., Meyer, V., & Ram, A. F. J. (2013). Autophagy promotes survival in aging submerged cultures of the filamentous fungus *Aspergillus niger*. *Applied Microbiology and Biotechnology*, 97(18), 8205–8218. <https://doi.org/10.1007/s00253-013-4971-1>
- Nitsche, B. M., Jørgensen, T. R., Akeroyd, M., Meyer, V., & Ram, A. F. J. (2012). The carbon starvation response of *Aspergillus niger* during submerged cultivation: Insights from the transcriptome and secretome. *BMC Genomics*, 13, 380. <https://doi.org/10.1186/1471-2164-13-380>
- Otsu, N. (1979). A threshold selection method from gray-level histograms. *Systems, Man and Cybernetics, IEEE Transactions on*, 9, 62–66.
- Papagianni, M. (2004). Fungal morphology and metabolite production in submerged mycelial processes. *Biotechnology Advances*, 22(3), 189–259.
- Pascual, S., Cal, A., de Magan, N., & Melgarejo, P. (2000). Surface hydrophobicity, viability and efficacy in biological control of *Penicillium oxalicum* spores produced in aerial and submerged culture. *Journal of Applied Microbiology*, 89(5), 847–853. <https://doi.org/10.1046/j.1365-2672.2000.01189.x>
- Posch, A. E., Spadiut, O., & Herwig, C. (2012). A novel method for fast and statistically verified morphological characterization of filamentous fungi. *Fungal Genetics and Biology*, 49(7), 499–510.
- Russ, J. (2016). *The image processing handbook* (7th ed.). CRC Press. <https://doi.org/10.1201/b18983>
- Schmideder, S., Barthel, L., Müller, H., Meyer, V., & Briesen, H. (2019). From three-dimensional morphology to effective diffusivity in filamentous fungal pellets. *Biotechnology and Bioengineering*, 116(12), 3360–3371. <https://doi.org/10.1002/bit.27166>
- Schmideder, S., Müller, H., Barthel, L., Friedrich, T., Niessen, L., Meyer, V., & Briesen, H. (2020). Universal law for diffusive mass transport through mycelial networks. *Biotechnology and Bioengineering*, 118(2), 930–943. <https://doi.org/10.1002/bit.27622>
- Schrinner, K., Veiter, L., Schmideder, S., Doppler, P., Schrader, M., Münch, N., Althof, K., Kwade, A., Briesen, H., Herwig, C., & Krull, R. (2020). Morphological and physiological characterization of filamentous *Lentzea aerocolonigenes*: Comparison of biopellets by microscopy and flow cytometry. *PLoS One*, 15(6), e0234125. <https://doi.org/10.1371/journal.pone.0234125>
- Tegelaar, M., Aerts, D., Teertstra, W. R., & Wösten, H. A. B. (2020). Spatial induction of genes encoding secreted proteins in micro-colonies of *Aspergillus niger*. *Scientific Reports*, 10(1), 1536. <https://doi.org/10.1038/s41598-020-58535-0>
- Van Leeuwen, M. R., Krijgheld, P., Bleichrodt, R., Menke, H., Stam, H., Stark, J., Wösten, H. A., & Dijksterhuis, J. (2013). Germination of conidia of *Aspergillus niger* is accompanied by major changes in RNA profiles. *Studies in Mycology*, 74(1), 59–70. <https://doi.org/10.3114/sim009>
- Veiter, L., & Herwig, C. (2019). The filamentous fungus *Penicillium chrysogenum* analysed via flow cytometry—A fast and statistically sound insight into morphology and viability. *Applied Microbiology and Biotechnology*, 103(16), 6725–6735. <https://doi.org/10.1007/s00253-019-09943-4>
- Veiter, L., Rajamanickam, V., & Herwig, C. (2018). The filamentous fungal pellet—Relationship between morphology and productivity. *Applied Microbiology and Biotechnology*, 102(7), 2997–3006.
- Willemse, J., Büke, F., van Dissel, D., Grevink, S., Claessen, D., & van Wezel, G. P. (2018). Sparticle, an algorithm for the analysis of filamentous microorganisms in submerged cultures. *Antonie Van Leeuwenhoek*, 111(2), 171–182. <https://doi.org/10.1007/s10482-017-0939-y>
- Wucherpennig, T., Hestler, T., & Krull, R. (2011). Morphology engineering—Osmolality and its effect on *Aspergillus niger* morphology and productivity. *Microbial Cell Factories*, 10, 58. <https://doi.org/10.1186/1475-2859-10-58>
- Wucherpennig, T., Kiep, K. A., Driouch, H., Wittmann, C., & Krull, R. (2010). Morphology and rheology in filamentous cultivations. In A. I. Laskin, S. Sariaslani, & G. M. Gadd (Eds.), *Advances in applied microbiology* (Vol. 72, pp. 89–136). Elsevier Academic Press Inc.
- Zacchetti, B., Willemse, J., Recter, B., van Dissel, D., van Wezel, G. P., Wösten, H. A. B., & Claessen, D. (2016). Aggregation of germlings is a major contributing factor towards mycelial heterogeneity of *Streptomyces*. *Scientific Reports*, 6, 27045. <https://doi.org/10.1038/srep27045>
- Zhang, J., & Zhang, J. (2016). The filamentous fungal pellet and forces driving its formation. *Critical Reviews in Biotechnology*, 36(6), 1066–1077.

SUPPORTING INFORMATION

Additional supporting information can be found online in the Supporting Information section at the end of this article.

How to cite this article: Müller, H., Barthel, L., Schmideder, S., Schütze, T., Meyer, V., & Briesen, H. (2022). From spores to fungal pellets: A new high-throughput image analysis highlights the structural development of *Aspergillus niger*. *Biotechnology and Bioengineering*, 119, 2182–2195. <https://doi.org/10.1002/bit.28124>